



City Research Online

City, University of London Institutional Repository

Citation: Axtmann, G., Rist, U., Hegner, F. & Bruecker, C. (2016). Numerical investigation of the bending of slenderwall-mounted cylinders in low reynolds number flow. Notes on Numerical Fluid Mechanics and Multidisciplinary Design, 132, pp. 191-201. doi: 10.1007/978-3-319-27279-5_17

This is the accepted version of the paper.

This version of the publication may differ from the final published version.

Permanent repository link: <https://openaccess.city.ac.uk/id/eprint/15113/>

Link to published version: https://doi.org/10.1007/978-3-319-27279-5_17

Copyright: City Research Online aims to make research outputs of City, University of London available to a wider audience. Copyright and Moral Rights remain with the author(s) and/or copyright holders. URLs from City Research Online may be freely distributed and linked to.

Reuse: Copies of full items can be used for personal research or study, educational, or not-for-profit purposes without prior permission or charge. Provided that the authors, title and full bibliographic details are credited, a hyperlink and/or URL is given for the original metadata page and the content is not changed in any way.

City Research Online:

<http://openaccess.city.ac.uk/>

publications@city.ac.uk

Numerical investigation of the bending of slender wall-mounted cylinders in low Reynolds number flow

Gabriel Axtmann, Ulrich Rist, Franziska Hegner and Christoph Bruecker

Abstract The aim of the present studies is construction of reference data for the prediction of the bending of sensor hairs close to the wall in a boundary-layer flow. Three-dimensional direct numerical simulations (DNS) of finite cylinders in single and tandem configuration are carried out. The numerical setup is guided by a towing-tank experiment performed at the Technical University of Freiberg. All numerical configurations are chosen to complement and extend the experimental work. The bending curve of the cylinders is estimated by a static approach according to 1st-order Euler-Bernoulli beam theory. Based on the forces, extrapolated from the DNS of the flow field, the influence of wall- and top-end effects and Reynolds numbers between 5 and 40 is examined more deeply. Also, varying positions of cylindrical tandem configurations in stream- and spanwise directions are investigated. The present work shows good agreement between simulation and experiment.

1 Introduction

With this work we want to contribute to a better understanding and theoretical prediction of so-called micro-pillar sensor arrays for detection of flow phenomena close to a wall, see *Bruecker et al.* [1]. The basic element of such a sensor array is a slender, wall-mounted circular cylinder of finite length at small Reynolds numbers which bends under the action of the fluid forces like a bristle. In practice, the deflection of the sensor tips can be measured by optical means and, once calibrated in a reference flow, converted to wall shear. Theoretically, the underlying processes are not well understood such that error characteristics and the influence of different parameters are not yet fully known.

G. Axtmann · U. Rist
Institute of Aerodynamics and Gas Dynamics, Pfaffenwaldring 21, 70569 Stuttgart, Germany
e-mail: axtmann@iag.uni-stuttgart.de

In flow over surfaces with attached micro-pillar sensors, the pillars interact with the flow by changing their orientation in response to the acting fluid forces. Typical fibers have a diameter of 20-50 μm and 40-500 μm length. The flow around a hair sensor is approximately the flow around a circular cylinder. Aspect ratios are varying between 2 and 25 while the Reynolds number is below 40. Analytical solutions for creeping flow around circular cylinders with $Re_d < 1$ are well-known [9]. Between $1 \leq Re \leq 47$ the flow field over a infinitely long cylinder normal to the flow direction separates with a recirculation region made up of two symmetrically placed vortices on each side of the symmetry plane [8]. This is highly affected by end-effects in the case of a finite-length cylinder [6]. Here, the aspect ratio of the finite cylinder effects the critical Reynolds number as well. *Norberg* [3] poured this into the relation: $Re_{d,crit} = 47.4 + 1.8 \times 10^3 (h/d)^{-2}$ with height h of the cylinder and its diameter d . According to this, the onset of vortex shedding for micro-pillars can be neglected up to: $h_{max}/d_{min} = 500/20 \Rightarrow Re_{d,crit} = 50.3$.

The study of the flow over two cylinders in tandem configuration is investigated very well for $Re_d > 40$. *Ohya et al.* [4] considered Reynolds numbers between 80 and 2.3×10^5 and cylinder spacings up to 30 diameters. They found out that the drag force is largely dependent on the Reynolds number and the spacing. Although there is a lot of previous work on single- and tandem configurations, the authors could not find research especially on tandem configurations for low Reynolds numbers in the range of 1-40. In this report, a numerical investigation of finite aspect ratio cylinders in a single- and tandem configuration for $5 \leq Re \leq 40$ is shown. The cylinders are wall-mounted on a flat plate. Calculation of bending due to fluid forces on surfaces are done according to 1st-order Euler-Bernoulli beam theory. This theory represents the static bending behaviour of the cylinder due to flow-induced forces on its surface. In tandem configuration, varying positions in streamwise and spanwise direction between $10d \leq dx \leq 18d$ and $1d \leq dy \leq 6d$, respectively, are examined.

2 Experimental setup and numerical method

Experiments were conducted in a towing-tank experiment at the Technical University of Freiberg, see Figure 1a). The circular cylinder is mounted on a horizontal moving plate. The length is 200 mm and its diameter 20 mm. This corresponds to an aspect ratio of 10. The measurements were performed for different Reynolds numbers, based on towing speed, cylinder diameter and viscosity of the fluid. For comparisons with the experiments, the numerical model is set up with a domain that extends from 50 diameters upstream to 75 diameters downstream of the cylinder. The lateral sides of the domain are implemented as slip walls and placed in a distance of 37.5 diameters from the center of the cylinder. The experimental top wall is located at 16 diameters distance parallel to the ground plate, see Figure 1b). An overview of the numerical boundary conditions is given in Table 1. The flow field around the single cylinder is discretized by a structured mesh, as shown in Figure 2a) for one wall-parallel plane. Equidistant wedge elements are used in the area around

Boundary	Type	Dirichlet Condition	Neumann Condition
inlet, outlet	patch	$u = u_\infty, p = 0$	$\delta p / \delta x = 0, \delta u / \delta x = 0$
sides, top	slip wall	$v = 0$	$\delta u / \delta y = \delta w / \delta y = \delta p / \delta y = 0$
bottom, cylinder	no-slip wall	$u = 0$	$\delta p / \delta x = 0$

Table 1: Numerical boundary conditions

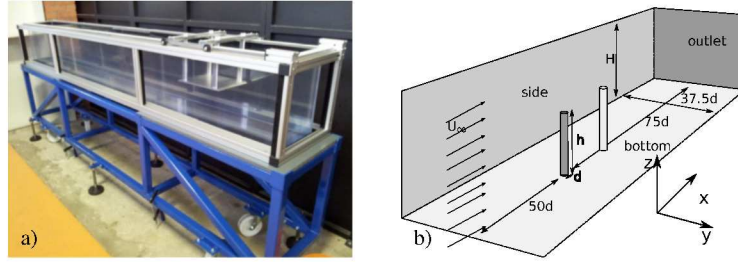


Fig. 1: a) Experimental setup of towing tank, b) Computational domain

the cylinder. The spatial boundary layer resolution is set up with 60 points. In the far field Cartesian grids are implemented. The finite end at the top of the cylinder is closed by a butterfly mesh. To avoid high aspect ratios in the tandem cylinder configurations, a hybrid meshing approach is applied there, as shown in Figure 2b). For

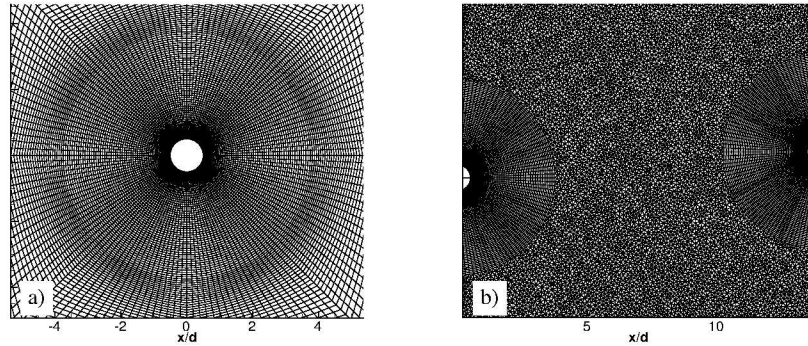


Fig. 2: a) 2D section of structured, b) 2D section of hybrid mesh for tandem configuration

solving the Navier-Stokes-Equations, the CFD Toolbox OpenFOAM is used. Due to the low Reynolds numbers for this study a laminar viscous fluid model is chosen, resulting in a direct numerical simulation. The inflow condition is a uniform block profile with a freestream velocity of $u_\infty = 1.0 \text{ m/s}$. Since $Ma \ll 0.3$, the density is

constant at $\rho = 1.0 \text{ kg/m}^3$. The outlet is modelled by a pressure outlet. A grid convergence study following *Roache* [5] was conducted to evaluate discretization errors with determination of the Grid Convergence Index (GCI). The error stays within an error-band of 0.5%. This shows a non significant influence of the discretization error and confirms the chosen mesh.

Quantifying the influence of wall-boundedness and geometrical domain restrictions, relevant parameters such as Reynolds number Re_d , mean drag coefficient $\overline{C_D}$ and blockage ratio BR are introduced in Equation (1).

$$Re_d = \frac{u_\infty d}{\nu}, \quad \overline{C_D} = \frac{\overline{F_d}}{1/2 \rho u_\infty^2 A_{ref}}, \quad BR = \frac{h}{H}, \quad (1)$$

where d is the diameter, ν the kinematic viscosity, F_d the force acting on the surface of the cylinder, A_{ref} the projected surface normal to the flow, h the height of the cylinder and H the height of the channel. As seen in Figure 3, the simulation results run somehow parallel to the prediction of *Tritton's* empirical ansatz for circular cylinders in 2D flow. The drag is up to 22 % higher for $Re_d < 5$ than *Tritton's* curve and decreases for $Re_d > 10$. The difference is caused by the three-dimensionality of the finite-cylinder flow together with wall end-effects. Therefore, the influence of the boundary layer of the ground plate is investigated for $Re_d = 10$. The drag decreases to 12% with no boundary layer and fits *Tritton's* curve. In comparison to the towing-tank experiments [2], the difference is around 1.8 % for $Re_d = 5$.

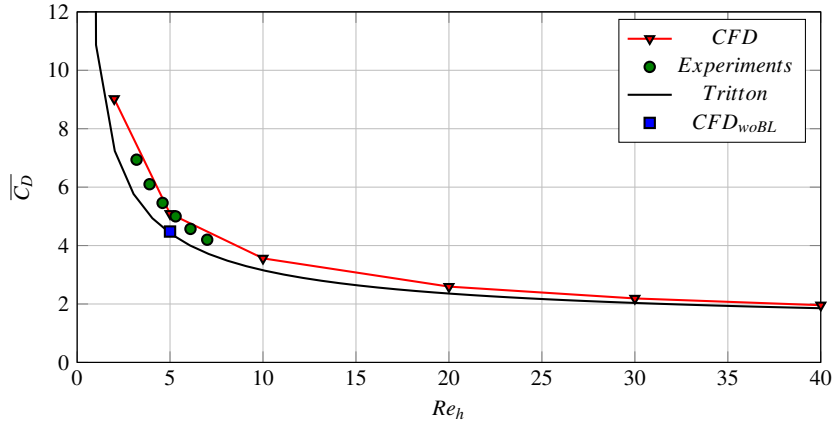


Fig. 3: $\overline{C_D}$ for single cylinder, towing-tank experiments [2] and *Tritton* [7]

With less blockage, i.e. decreasing blockage ratio BR , the maximal u -velocity above the tip at $z/d = 11$ is reduced by 11 %, as seen in Figure 4a). This also affects the mean drag $\overline{C_D}$, as seen in Figure 4b). The mean drag grows linearly with blockage ratio. For $BR = 0.6$, the resulting $\overline{C_D}$ is 3.6 and 14 % higher than *Tritton's* experimental data.

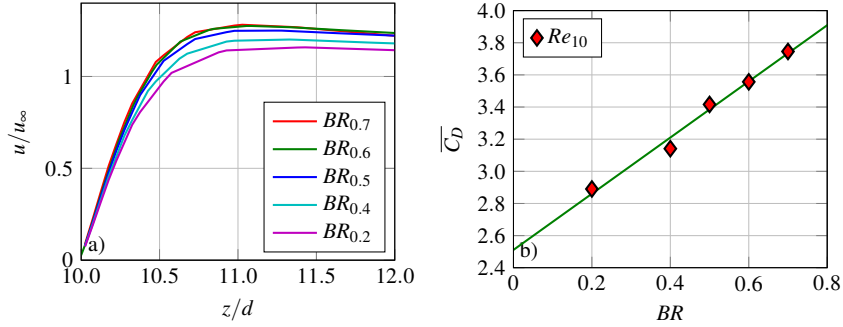


Fig. 4: a) u/u_∞ at $y/d = 0$, b) $\overline{C_D}$ for different blockage ratios BR

3 Results and discussion

3.1 Influence of Reynolds number on single cylinder

Next, the Reynolds number is varied between $Re_d = 5$ and 40. As seen in Figure 5a), the flow for $Re_d = 5$ contains almost no regions of flow separation. The streamlines diverge as they approach the cylinder, wrap around and re-contract downstream, similar to two-dimensional flow. Small three-dimensional effects occur at the top and at the bottom of the cylinder, due to the boundary layer on the ground plate of the cylinder and around the tip. Along the frontal stagnation line there is a downwash effect, while an upwash effect is observed on the rear side. At Reynolds number $Re_d = 40$, the wake behind the cylinder increases dramatically, see Figure 5b). Quasi 2D flow behind the cylinder is no longer existent and a separation bubble develops over the whole length of the cylinder.

To better understand the three-dimensionality and the influence of the tip vortex, the velocity distribution on the symmetry plane $y/d = 0$ of the cylinder is visualized in Figures 5c)+d). For $Re_d = 5$, the flow shows no separation at the tip of the cylinder and resembles creeping flow. The rear stagnation point is slightly below the top end of the cylinder and the flow resembles a backward facing step flow. For higher Reynolds numbers, two separation zones on the rear side are arising, as seen in Figure 5d) for $Re_d = 40$. The flow contains a huge tip separation bubble as long as one third of the cylinder length and a further separation zone from the ground plate.

Now, the bending of the cylinder, due to local drag forces by pressure F_p and friction F_f , is investigated sectionwise along the wall-normal coordinate, using Equation (2):

$$F_p(z) = \int_S (p(z) - p_\infty) \cdot \hat{n} \cdot \hat{i} dA, \quad F_f(z) = \int_S \tau_w(z) \cdot \hat{i} \cdot \hat{i} dA, \quad (2)$$

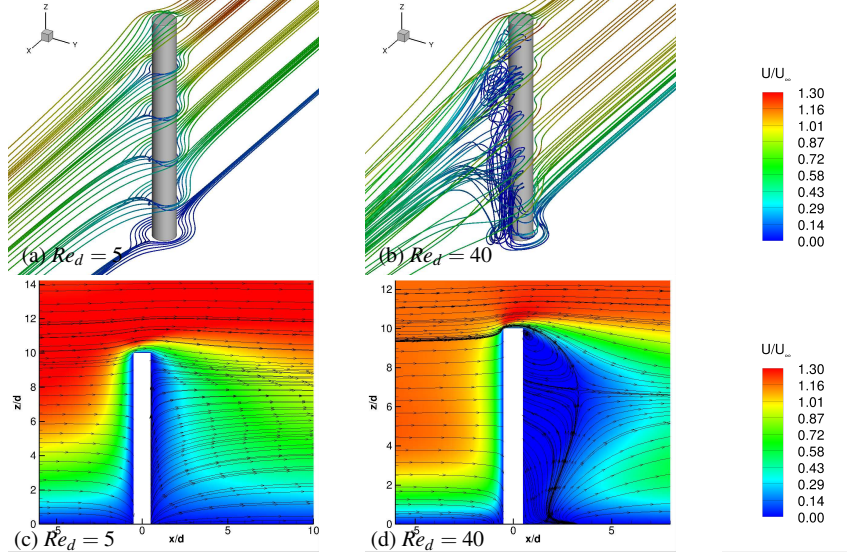


Fig. 5: u/u_∞ for finite, wall-mounted single cylinder at $Re_d = 5$ and $Re_d = 40$

where p_∞ is the ambient pressure, \hat{n} the vector normal to the surface with area dA , \hat{i} the unit vector normal to the surface, τ_w the shear stress acting on the surface and \hat{t} the tangential vector relative to the surface. The non-dimensional drag coefficients are defined as follows:

$$c_p(z) = \frac{F_p(z)}{1/2 * \rho * u_{loc}(z)^2 * L * d}, \quad c_f(z) = \frac{F_f(z)}{1/2 * \rho * u_{loc}(z)^2 * L * d}, \quad C_D(z) = c_p(z) + c_f(z), \quad (3)$$

where $u_{loc}(z)$ is the case-dependent Blasius boundary-layer similarity solution, L the sectional reference length and d the diameter of the cylinder. The variation of pressure along the cylinder length generates a non-linear section-dependent force. This leads to the drag curve, shown in Figure 6a. For better comparison, all curves are normalized by $u_{loc}(z)$ of each case. The aspect ratio is 10. Intuitively, an influence of wall effects on the bottom and at the tip of the cylinder is expected. Accordingly, the lower local velocity in the boundary layer leads to higher drag at the bottom (zone 1) which decreases towards the top. The drag peak at the top (zone 3) of the cylinder is different, caused by a non-linear shear stress dependency on Reynolds number, as shown in Figure 6b). Overall, the general drag curve is lowering with higher Reynolds numbers, see Figure 6c).

The static bending curve $w(z)$ of the cylinder is computed from the local drag coefficient by 1st order Euler-Bernoulli theory, using Equation (4):

$$\frac{d^2}{dz^2} \left(EI \frac{d^2 w(z)}{dz^2} \right) = q(z) \quad (4)$$

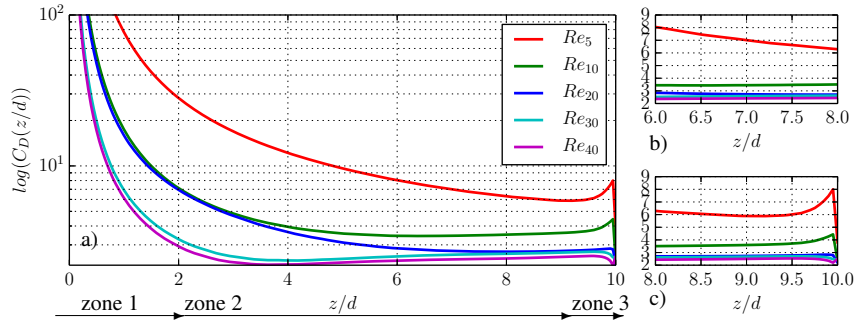


Fig. 6: a) $\log(C_D(z))$, b) $C_D(z/d)$ for $6 < z/d < 8$, c) $C_D(z/d)$ for $8 < z/d < 10$

with the following boundary conditions:

$$\begin{aligned} Q(h) = 0 &\rightarrow C_1, & \varphi(0) = 0 &\rightarrow C_3 = 0, \\ M(h) = 0 &\rightarrow C_2, & w(0) = 0 &\rightarrow C_4 = 0, \end{aligned} \quad (5)$$

where $q(z)$ is the distributed load, $Q(z)$ the shear force, $M(z)$ the bending moment, $\varphi(z)$ the bending angle and $w(z)$ the deflection of the beam. Bending near the ground plate is nearly neglectable and hence independent of Re_d , as seen in Figure 7. Towards the tip of the cylinder, a linear bending of the cylinder is observed. The maximal bending is calculated for $Re_d = 40$ whereas towards $Re_d = 5$ the bending curve decreases.

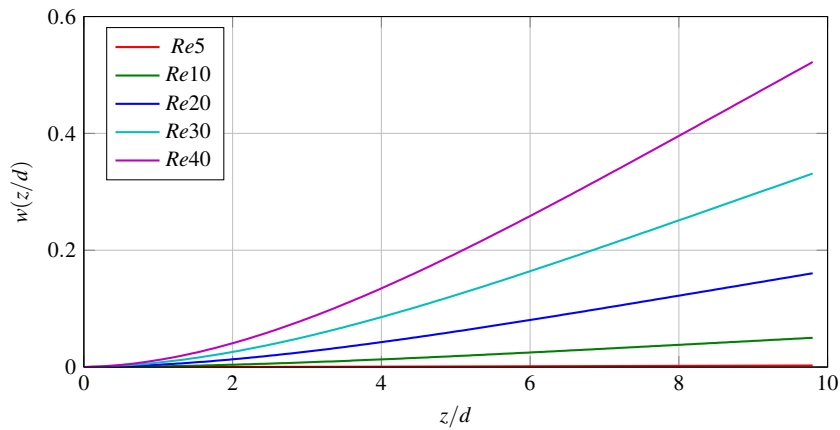


Fig. 7: Static bending curve $w(z/d)$ for $5 \leq Re \leq 40$

3.2 Tandem configuration

In this section, a tandem configuration is investigated for various distances between the two cylinders in stream- and spanwise direction. The streamwise distance is set to $dx = 10d, 14d, 18d$ and $26d$ at $Re_d = 10$. The local drag $C_D(z/d)$ and bending $w(z)$ are calculated in analogy to the previous section. Figure 8 shows the rear side of the first and second cylinder for the tandem configuration with $dx = 10d$ and $dx = 18d$. Reverse-flow zones for each cylinder are visualized by the isosurface at $u/u_\infty = 0$. The reverse-flow zones of the first cylinder are similar, while those for the second cylinder increase with higher distance dx .

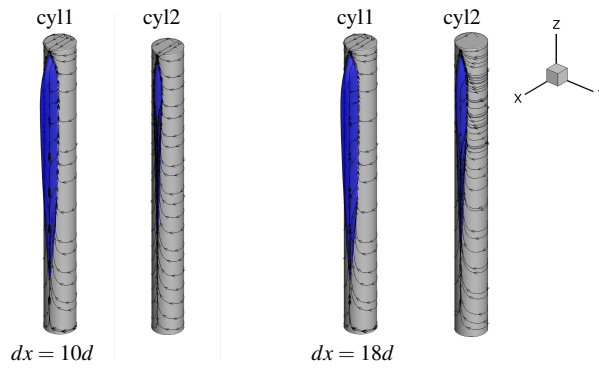


Fig. 8: Reverse-flow zones behind cylinders in tandem configuration $dx = 10d$ (left) and $18d$ (right)

Figure 9a) shows the mean drag coefficient $\overline{C_{D_T}}$ of the tandem configuration normalized by the mean drag $\overline{C_{D_S}}$ of an isolated cylinder. The mean drag of the first cylinder of the tandem configuration is slightly lower than for an isolated cylinder, dependent on the distance dx . The cause of this drag reduction is that the downstream cylinder affects the upstream cylinder's wake when the two cylinders are in close proximity. With increasing distance dx the wake of the first cylinder becomes weaker and the drag of the second one increases towards the drag of the isolated cylinder, as seen in Figure 9a). The drag coefficients $C_D(z/d)$ for the second cylinders are compared in Figure 9b). The largest influence of the wake of the first cylinder occurs over the midspan area of the cylinder. The bending curves of the second cylinder follow the local drag distribution. With increasing dx the bending of the second cylinder increases, see Figure 9c).

The spanwise variation for $dy = 0d, 1d, 2d, 4d$ and $6d$ of the tandem configuration is investigated for $Re_d = 10$ at $dx = 14d$. For $dy \leq 4d$ the total drag of the first cylinder is slightly lower than for the single cylinder, as seen in Figure 10a). For $dy = 1d$ the drag for the second cylinder is around 32 % less than for the isolated cylinder and linearly increases towards $dy = 4d$. This changes at $dy = 6d$, where even slightly

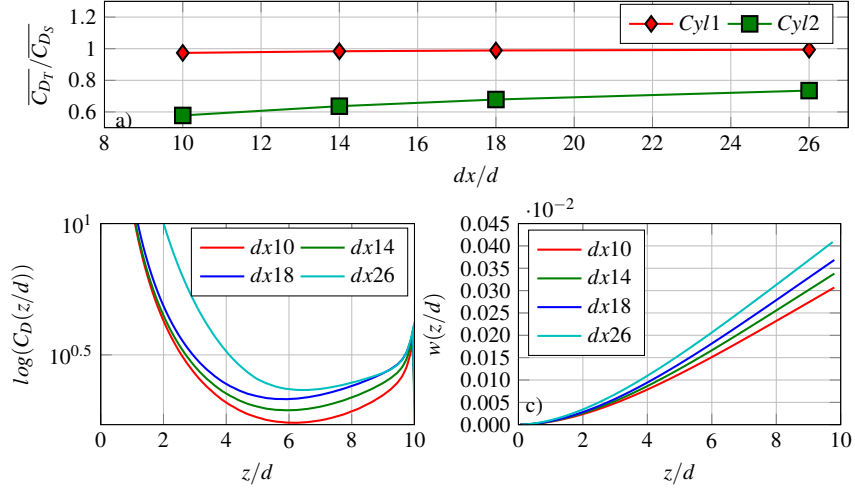


Fig. 9: a) $\overline{C_{D_T}}/\overline{C_{D_S}}$ b) $\log(C_D(z/d))$ 2nd Cyl. c) $w(z/d)$ 2nd Cyl., : $dx = 10d - 26d$

higher drag than for the first one is observed. In this last case the second cylinder has practically left the influence of the first cylinder. The local drag $C_D(z/d)$ increases for $dy = 0d$ towards $dy = 6d$, see Figure 10b). The bending curves of the beam follow these results, as seen in Figure 10c).

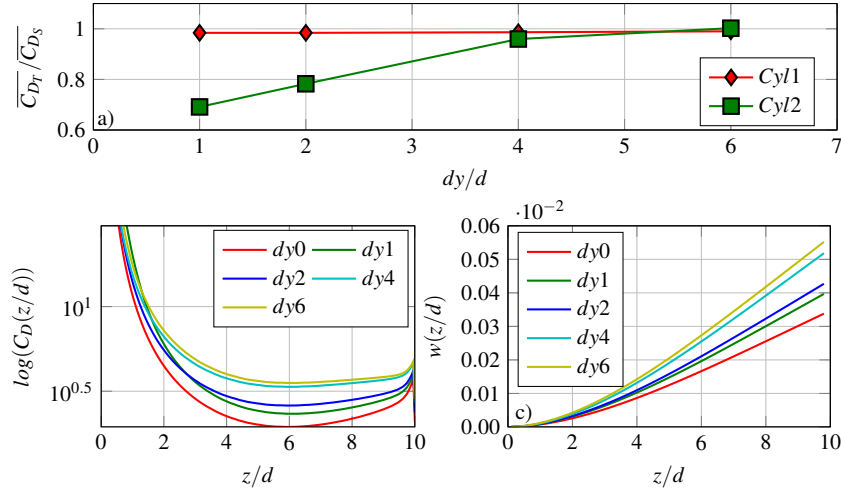


Fig. 10: a) $\overline{C_{D_T}}/\overline{C_{D_S}}$ b) $\log(C_D(z/d))$ 2nd Cyl. c) $w(z/d)$ 2nd Cyl., : $dy = 0d - 6d$

4 Conclusions and Outlook

The present work has shown that the streamwise forces acting on a wall-mounted, thin, slender, circular cylinder in a steady, viscous shear flow below $Re_d \approx 40$ are very close to those of circular cylinders in two-dimensional flow which is well-documented in textbooks. Wall and free-end effects which are fully included in the present direct numerical simulations have only a local influence on the flow forces without significance for the bending of the cylinder, which is also corroborated by the observed good agreement of the present results with experiments performed at TU Freiberg. These observations have important consequences for the continuation of the present project. Direct numerical simulation of a boundary layer containing a micro-pillar sensor array is still impossible because of the widely different scales between the size of the integration domain, the different sizes of eddies in the flow and the cylinder diameters. The present results imply that displacements of ideal sensors can be faithfully computed with one-dimensional beam theory using the velocity extracted along the cylinder's center line from a fluid-flow simulation without cylinders. This will solve the first part of the otherwise intractable fluid-structure interaction-problem related to micro-pillar sensors. The second part, i.e., the interaction of the sensors with the flow and hence with each other will be treated by imposing appropriate body forces in the fluid-flow simulation.

References

- [1] Bruecker C, Bauer D, Chaves H (2007) Dynamic response of micro-pillar sensors measuring fluctuating wall-shear-stress. *Experiments of Fluids* 42:737–749
- [2] Luehr A, Hegner F (2014) Characterization of the beam bending of a sensor pillar. IMFD TU Freiberg
- [3] Norberg C (1994) An experimental investigation of the flow around a circular cylinder. *Journal of Fluid Mechanics* 258:287–346
- [4] Ohya Y, Okajima A, Hayashi M (1989) *Wake Interference and Vortex Shedding*. Gulf Publishing
- [5] Roache P (1997) Quantification of uncertainty in computational fluid dynamics. *Annual Review of Fluid Mechanics* 29:60–126
- [6] Sen S (2009) Numerical simulation of steady flow past a circular cylinder. *Journal of Fluid Mechanics* 620:89–119
- [7] Tritton D (1959) Experiments on the flow past a circular cylinder at low reynolds numbers. *Journal of Fluid Mechanics* 6:547–567
- [8] Williamson C (1996) Vortex dynamics in the cylinder wake. *Annual Review of Fluid Mechanics* 28:477–539
- [9] Zdravkovich M (2003) *Flow around circular cylinders*. New York Oxford University Press 2